

Thermal freeze-out versus chemical freeze-out reexamined

Dariusz Prorok

*Institute of Theoretical Physics, University of Wrocław,
Pl. Maka Borna 9, 50-204 Wrocław, Poland*

(Dated: December 6, 2007)

A competitive, to the commonly used blast-wave, model describing the freeze-out hypersurface is applied to fit the p_T -spectra of identified hadrons measured at relativistic heavy-ion collisions at $\sqrt{s_{NN}} = 62.4, 130$ and 200 GeV. Decays of resonances are taken into account completely. It has turned out that the fitted kinetic freeze-out temperature and baryon number chemical potential depend weakly on the centrality of the collision and their values are close to the chemical freeze-out values determined from fits to particle yield ratios.

PACS numbers: 25.75.-q, 25.75.Dw, 24.10.Pa, 24.10.Jv

I. INTRODUCTION

During a heavy-ion collision a hot and dense medium is created which eventually evolves into a state of freely streaming particles. The process of hadron decoupling is called *freeze-out* and two kinds of freeze-out are distinguished [1, 2]: (i) *chemical freeze-out* at T_{chem} when the hadron abundances become fixed and (ii) *thermal (kinetic) freeze-out* at T_{kin} when elastic rescattering processes cease and hadrons start to escape freely. And $T_{chem} \geq T_{kin}$ is expected. Values of the statistical parameters at the chemical freeze-out are determined from fits to particle yield ratios, whereas corresponding values at the kinetic freeze-out are fitted to the spectra of hadrons. $T_{chem} \sim 150 - 170$ MeV is estimated at highest heavy-ion reaction energy [3, 4, 5, 6, 7, 8, 9, 10, 11, 12, 13]. Additionally, fits done for various centrality classes have revealed that T_{chem} is almost independent of centrality [4, 6, 8, 9, 10]. On the contrary, the temperature at the kinetic freeze-out depends on the centrality and is substantially lower. From the most central to the peripheral bin it changes as follows: $T_{kin} = 121 - 161$ MeV for PHENIX at $\sqrt{s_{NN}} = 130$ GeV [14], $T_{kin} = 111 - 147$ MeV for PHENIX at $\sqrt{s_{NN}} = 200$ GeV [15], $T_{kin} = 89 - 129$ MeV for STAR at $\sqrt{s_{NN}} = 200$ GeV [9] and $T_{kin} = 110 - 115$ MeV for BRAHMS at $\sqrt{s_{NN}} = 200$ GeV [16]. For the PHOBOS data at $\sqrt{s_{NN}} = 62.4$ GeV $T_{kin} = 103, 102, 101$ MeV for the central, mid-peripheral and peripheral bin, respectively [17]. However, the aforementioned estimates of T_{kin} have been done within the very simplified hydrodynamic model, *i.e.* the blast-wave model [18].

In this paper, we will show that the behavior of T_{kin} is model dependent and within a different hypersurface and with complete treatment of resonance decays different conclusions about statistical parameters at the kinetic freeze-out can be obtained. Namely, the statistical parameters at the kinetic freeze-out are roughly centrality independent and their values are close to the corresponding values at the chemical freeze-out.

II. FOUNDATIONS OF THE MODEL

The model applied here is inspired by the single-freeze-out model of Refs. [19, 20], but its main assumption about the simultaneous occurrence of chemical and thermal freeze-outs *is not postulated*. The assumptions of the present model are as follows. A noninteracting gas of stable hadrons and resonances at chemical and thermal equilibrium appears at the latter stages of a heavy-ion collision. The gas cools and expands, and after reaching the freeze-out point it ceases. The conditions for the freeze-out are expressed by values of two independent thermal parameters: T and μ_B . The strangeness chemical potential μ_S is determined from the requirement that the overall strangeness equals zero. All confirmed resonances up to a mass of 2 GeV from the Particle Data Tables [21], together with stable hadrons, are constituents of the gas. The freeze-out hypersurface is defined by the equation

$$\tau = \sqrt{t^2 - r_x^2 - r_y^2 - r_z^2} = const. \quad (1)$$

The four-velocity of an element of the freeze-out hypersurface is proportional to its coordinate

$$u^\mu = \frac{x^\mu}{\tau} = \frac{t}{\tau} \left(1, \frac{r_x}{t}, \frac{r_y}{t}, \frac{r_z}{t} \right). \quad (2)$$

The following parameterization of the hypersurface is chosen:

$$t = \tau \cosh \alpha_{\parallel} \cosh \alpha_{\perp}, \quad r_x = \tau \sinh \alpha_{\perp} \cos \phi, \quad r_y = \tau \sinh \alpha_{\perp} \sin \phi, \quad r_z = \tau \sinh \alpha_{\parallel} \cosh \alpha_{\perp}, \quad (3)$$

where α_{\parallel} is the rapidity of the element, $\alpha_{\parallel} = \tanh^{-1}(r_z/t)$, and α_{\perp} controls the transverse radius:

$$r = \sqrt{r_x^2 + r_y^2} = \tau \sinh \alpha_{\perp}. \quad (4)$$

The transverse size is restricted by the condition $r < \rho_{max}$. τ and ρ_{max} constitute two geometric parameters of the model. The maximum transverse-flow parameter (or the surface velocity) is given by

$$\beta_{\perp}^{max} = \frac{\rho_{max}}{\sqrt{\tau^2 + \rho_{max}^2}} = \frac{\rho_{max}/\tau}{\sqrt{1 + (\rho_{max}/\tau)^2}}. \quad (5)$$

The invariant distribution of the measured particles of species i has the form [19, 20]

$$\frac{dN_i}{d^2p_T dy} = \int p^{\mu} d\sigma_{\mu} f_i(p \cdot u), \quad (6)$$

where $d\sigma_{\mu}$ is the normal vector on a freeze-out hypersurface, $p \cdot u = p^{\mu} u_{\mu}$, u_{μ} is the four-velocity of a fluid element and f_i is the final momentum distribution of the particle in question. The final distribution means here that f_i is the sum of primordial and simple and sequential decay contributions to the particle distribution. All contributions from weak decays are included. The primordial part of f_i is given by a Bose-Einstein or a Fermi-Dirac distribution at the kinetic freeze-out. A decay contribution is a one-dimensional or multidimensional integral of the momentum distribution of a decaying resonance (the exact formulae are obtained from the elementary kinematics of a many-body decay or the superposition of such decays, for details see [22] and the Appendix in [23]). The resonance is a constituent of the hadron gas and its distribution is also given by the Bose-Einstein (Fermi-Dirac) distribution function. Therefore the final distribution f_i depends explicitly on T and μ_B .

With the use of Eqs. (2) and (3), the invariant distribution (6) takes the following form:

$$\frac{dN_i}{d^2p_T dy} = \tau^3 \int_{-\infty}^{+\infty} d\alpha_{\parallel} \int_0^{\rho_{max}/\tau} \sinh \alpha_{\perp} d(\sinh \alpha_{\perp}) \int_0^{2\pi} d\xi p \cdot u f_i(p \cdot u), \quad (7)$$

where

$$p \cdot u = m_T \cosh(\alpha_{\parallel} - y) \cosh \alpha_{\perp} - p_T \cos \xi \sinh \alpha_{\perp}. \quad (8)$$

The model has four parameters, the two thermal parameters, the temperature T and the baryon number chemical potential μ_B , and the two geometric parameters, τ and ρ_{max} . It should be stressed that now all parameters of the model are fitted simultaneously, opposite to the case of Refs. [19, 20] where the determination proceeded in two steps. First, statistical parameters T and μ_B were fitted with the use of the experimental ratios of hadron multiplicities at midrapidity. Then geometric parameters were determined from fits to the transverse-momentum spectra. Therefore the assumption that the chemical freeze-out happens simultaneously with the kinetic freeze-out (the single freeze-out) was crucial in that approach. Now all parameters are fitted to the spectra, so the aforementioned assumption is not necessary and values of statistical parameters have the meaning of the values at the kinetic freeze-out.

With the use of Eq. (7) the measured transverse-momentum spectra of π^{\pm} , K^{\pm} , p and \bar{p} [9, 14, 16, 17, 24] can be fitted to determine values of the parameters of the model (data points with $p_T > 3$ GeV have been excluded). Fits are performed with the help of the χ^2 method. For the k th measured quantity R_k^{exp} and its theoretical equivalent $R_k^{th}(\alpha_1, \dots, \alpha_l)$, which depends on l parameters $\alpha_1, \dots, \alpha_l$, the χ^2 function is defined as

$$\chi^2(\alpha_1, \dots, \alpha_l) = \sum_{k=1}^n \frac{(R_k^{exp} - R_k^{th}(\alpha_1, \dots, \alpha_l))^2}{\sigma_k^2}, \quad (9)$$

where σ_k is the error of the k th measurement and n is the total number of data points. The fitted (optimum) values of parameters mean the values at which χ^2 has a minimum.

TABLE I: Values of the statistical and geometric parameters of the model for various centrality bins fitted with the use of the RHIC final data for the p_T spectra of identified charged hadrons [9, 14, 16, 24]. All data are at midrapidity, except the PHOBOS case (first three rows) where data are at $y = 0.8$ [17].

Au-Au collision case	Centrality [%]	N_{part}	T_{kin} [MeV]	μ_B [MeV]	ρ_{max} [fm]	τ [fm]	β_{\perp}^{max}	χ^2/NDF	NDF
PHOBOS at $\sqrt{s_{NN}} = 62.4$ GeV	0-15	294.0	148.52 \pm 1.15	72.60 \pm 3.81	7.84 \pm 0.19	8.35 \pm 0.14	0.684 \pm 0.006	0.995	72
	15-30	175.0	149.64 \pm 1.42	69.47 \pm 4.13	6.23 \pm 0.19	7.20 \pm 0.17	0.654 \pm 0.007	0.43	72
	30-50	88.0	151.29 \pm 1.70	67.15 \pm 4.47	4.60 \pm 0.18	6.05 \pm 0.18	0.605 \pm 0.009	0.20	71
PHENIX at $\sqrt{s_{NN}} = 130$ GeV	0-5	347.7	166.74 \pm 3.96	35.06 \pm 8.97	6.31 \pm 0.41	8.08 \pm 0.44	0.616 \pm 0.014	0.53	78
	5-15	271.3	161.70 \pm 3.21	43.14 \pm 7.77	6.34 \pm 0.35	7.57 \pm 0.34	0.642 \pm 0.012	0.46	78
	15-30	180.2	162.33 \pm 3.29	38.52 \pm 7.75	5.32 \pm 0.29	6.54 \pm 0.29	0.631 \pm 0.012	0.50	78
	30-60	78.5	162.25 \pm 3.46	31.80 \pm 7.87	3.77 \pm 0.23	4.95 \pm 0.23	0.606 \pm 0.015	0.75	78
	60-92	14.3	159.46 \pm 6.85	37.05 \pm 16.09	1.87 \pm 0.27	3.26 \pm 0.27	0.496 \pm 0.043	1.37	42
	0-5	351.4	150.07 \pm 1.34	24.10 \pm 3.66	9.28 \pm 0.21	9.48 \pm 0.19	0.699 \pm 0.004	0.69	122
PHENIX at $\sqrt{s_{NN}} = 200$ GeV	5-10	299.0	150.18 \pm 1.35	23.48 \pm 3.65	8.75 \pm 0.20	8.80 \pm 0.18	0.705 \pm 0.004	0.50	122
	10-15	253.9	150.16 \pm 1.35	22.75 \pm 3.65	8.25 \pm 0.19	8.20 \pm 0.17	0.709 \pm 0.004	0.37	122
	15-20	215.3	150.00 \pm 1.36	22.38 \pm 3.65	7.80 \pm 0.18	7.69 \pm 0.16	0.712 \pm 0.004	0.37	122
	20-30	166.6	149.59 \pm 1.31	24.03 \pm 3.47	7.13 \pm 0.16	6.96 \pm 0.14	0.716 \pm 0.004	0.45	122
	30-40	114.2	149.79 \pm 1.36	23.78 \pm 3.56	6.14 \pm 0.14	6.03 \pm 0.12	0.713 \pm 0.004	0.66	122
	40-50	74.4	148.53 \pm 1.40	22.52 \pm 3.71	5.28 \pm 0.13	5.27 \pm 0.11	0.708 \pm 0.005	0.89	122
	50-60	45.5	147.75 \pm 1.51	22.02 \pm 4.03	4.38 \pm 0.12	4.55 \pm 0.10	0.694 \pm 0.005	0.96	122
	60-70	25.7	144.57 \pm 1.65	21.63 \pm 4.56	3.63 \pm 0.11	3.91 \pm 0.09	0.680 \pm 0.006	1.12	122
	70-80	13.4	141.77 \pm 1.98	24.13 \pm 5.68	2.84 \pm 0.10	3.22 \pm 0.09	0.662 \pm 0.008	1.23	122
	80-92	6.3	140.62 \pm 2.46	14.29 \pm 7.12	2.24 \pm 0.10	2.77 \pm 0.09	0.630 \pm 0.011	1.13	122
STAR at $\sqrt{s_{NN}} = 200$ GeV	0-5	352.0	159.99 \pm 1.19	24.00 \pm 2.17	9.22 \pm 0.31	7.13 \pm 0.19	0.791 \pm 0.006	0.30	71
	5-10	299.0	160.58 \pm 1.16	24.97 \pm 2.17	8.34 \pm 0.28	6.75 \pm 0.18	0.777 \pm 0.006	0.27	71
	10-20	234.0	161.20 \pm 1.14	22.91 \pm 2.15	7.45 \pm 0.24	6.17 \pm 0.16	0.770 \pm 0.006	0.22	73
	20-30	166.0	162.27 \pm 1.12	23.05 \pm 2.17	6.31 \pm 0.20	5.60 \pm 0.14	0.748 \pm 0.007	0.25	75
	30-40	115.0	161.97 \pm 1.08	20.43 \pm 2.17	5.38 \pm 0.17	5.15 \pm 0.12	0.722 \pm 0.007	0.19	75
	40-50	76.0	162.97 \pm 1.08	21.01 \pm 2.21	4.46 \pm 0.14	4.64 \pm 0.11	0.693 \pm 0.008	0.13	75
	50-60	47.0	163.41 \pm 1.07	18.75 \pm 2.25	3.67 \pm 0.12	4.13 \pm 0.10	0.664 \pm 0.008	0.13	75
	60-70	27.0	162.39 \pm 1.06	16.47 \pm 2.31	2.95 \pm 0.10	3.79 \pm 0.09	0.614 \pm 0.010	0.26	75
	70-80	14.0	163.70 \pm 1.15	15.84 \pm 2.50	2.22 \pm 0.09	3.16 \pm 0.08	0.574 \pm 0.012	0.61	75
BRAHMS at $\sqrt{s_{NN}} = 200$ GeV	0-10	328.0	150.60 \pm 1.39	23.07 \pm 3.51	9.26 \pm 0.25	8.65 \pm 0.21	0.731 \pm 0.004	0.43	114
	10-20	239.0	151.38 \pm 1.48	26.53 \pm 3.72	8.07 \pm 0.23	7.68 \pm 0.19	0.724 \pm 0.005	0.42	114
	20-40	140.0	149.43 \pm 1.54	25.92 \pm 3.98	7.00 \pm 0.21	6.73 \pm 0.17	0.721 \pm 0.005	0.26	112
	40-60	62.0	148.36 \pm 2.02	26.69 \pm 5.21	5.02 \pm 0.20	5.38 \pm 0.17	0.683 \pm 0.008	0.52	112

III. RESULTS

The fitted results for T_{kin} , μ_B , ρ_{max} and τ are gathered in Table I together with values of the surface velocity β_{\perp}^{max} and values of χ^2/NDF for each centrality class additionally characterized by the number of participants N_{part} . Errors are expressed by one standard deviation (1σ). Note that except the most peripheral bins of the PHENIX measurements all fits are statistically significant. That these new higher values of temperature (higher in comparison with the blast-wave fit values) are at minima is shown in Fig. 1 in an example of the temperature dependence of χ^2 for the PHENIX most central bin at $\sqrt{s_{NN}} = 200$ GeV. The simulation of the dependence was done within the same procedure as in the original single-freeze-out model, with the overall fixed value of $\mu_B = 27.5$ MeV (the average of values from [8, 12]) and the temperature fixed at each point and taken from the range 120-180 MeV with the 1 or 2 MeV step. Then two geometric parameters were fitted and χ^2 at their values was put into the figure.

Coming back to the results of simultaneous fits of all four parameters, some 1σ and 2σ contours are presented in Figs. 2 and 3. These contours are done in T_{kin} and β_{\perp}^{max} plains to make them comparable with the blast-wave results.

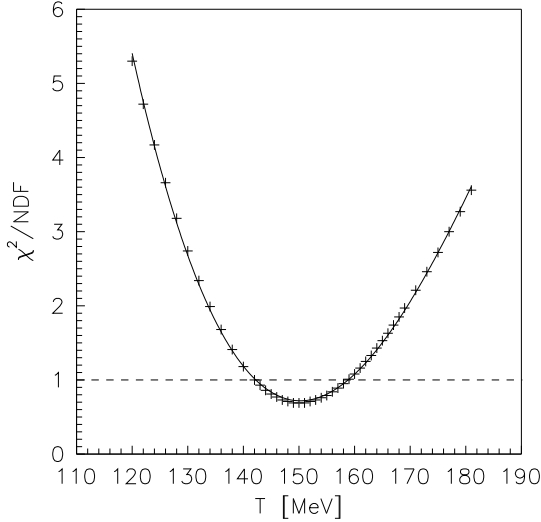


FIG. 1: Simulation of the temperature dependence of χ^2/NDF for PHENIX at $\sqrt{s_{NN}} = 200$ GeV and the 0 – 5% centrality class. Solid line is the polynomial 3 best fit.

But since the parameter space is four dimensional, the n -sigma contour is in fact the 3-dimensional ellipsoid imbedded in this space, so it can be presented only by means of its projections on some plains. Contours presented in Figs. 2 and 3 are such projections onto T_{kin} and β_{\perp}^{max} plains chosen at some fixed μ_B and τ , namely at their optimum values $\mu_{B,opt}$ and τ_{opt} , Fig. 2, and at $\mu_B = \mu_{B,opt} \pm 0.5\sigma_{\mu}$ and $\tau = \tau_{opt} \pm 0.5\sigma_{\tau}$, Fig. 3. In the right panel of Fig. 2, all examples are for most peripheral bins, except the PHENIX case at $\sqrt{s_{NN}} = 130$ GeV which is for the second from the most peripheral class. This is because errors in the case of the most peripheral bin of the PHENIX measurements at $\sqrt{s_{NN}} = 130$ GeV are substantially greater (see Table I), which results in too big extension of 1σ and 2σ contours (~ 3 times bigger than in the second from the most peripheral case). This fact together with χ^2/NDF much higher than 1 does not enable to determine firm optimum values of T_{kin} and β_{\perp}^{max} in this case. Generally, χ^2 is flatter in the vicinity of the optimum points in the PHENIX case at $\sqrt{s_{NN}} = 130$ GeV, as one can notice from Figs. 2 and 3. This is also expressed by ~ 2 times greater errors of the fitted values in this case. For other experiments 1σ and 2σ contours are relatively small. Their sizes do not change visibly from most central to mid-central bins and then increase gradually up to the sizes of the contours for most peripheral bins (in fact this behavior reflects the behavior of the corresponding errors, cf. Table I).

The feeding from weak decays is treated in the same way as experimental groups do, except the STAR case. So, for the PHENIX collisions at $\sqrt{s_{NN}} = 200$ GeV protons (antiprotons) from Λ ($\bar{\Lambda}$) decays are excluded. In the PHOBOS case protons (antiprotons) from Λ and Σ^+ ($\bar{\Lambda}$ and $\bar{\Sigma}^-$) decays are not counted. As far as the STAR case is considered, this Collaboration claims that its pion spectra are corrected for weak decays [9]. However, it has been shown that the best quality of the fit expressed by the value of χ^2/NDF is for full feeding from weak decays in this case [25]. This was done within the single-freeze-out scheme, but since here the freeze-out hypersurface and the description of decays are exactly the same, the full feeding from weak decays for the STAR case is assumed in calculations as well.

Results for T_{kin} and μ_B are also depicted as functions of N_{part} in Figs. 4 and 5, respectively. It is clearly seen that both T_{kin} and μ_B are almost independent of the collision centrality, only for peripheral bins some dependence can be observed. Additionally, their values are very close to the values at the chemical freeze-out. Namely, $T_{chem} = 165 - 169$ MeV and $\mu_B = 33 - 38$ MeV from the peripheral to most central bin at $\sqrt{s_{NN}} = 130$ GeV was found in Ref. [6], $T_{chem} \approx 155$ MeV and $\mu_B \approx 26$ MeV independent of the centrality for PHENIX at $\sqrt{s_{NN}} = 200$ GeV in Ref. [8] and $T_{chem} \approx 160$ MeV independent of the centrality and $\mu_B = 15 - 24$ MeV from the peripheral to most central bin for STAR at $\sqrt{s_{NN}} = 200$ GeV in Refs. [9, 10, 11].

In Figs. 6-10 measured and predicted spectra of identified hadrons are presented for some collisions at RHIC. In Fig. 6 the case of PHOBOS at $\sqrt{s_{NN}} = 62.4$ GeV is dealt with. The way as data and results are depicted is suggested by the PHOBOS analysis [17] (see Fig. 7 there). The lines are predictions of the present model done with the use of fitted parameters tabulated in Table I. But fits were done within intermediate ranges of p_T , that is in the ranges where single charged hadron data exists. Then predictions were made for sums of negatively and positively charged hadrons of the same kind but in the whole accessible ranges, namely ranges extended to the very low p_T where separate data on the summed yields exist. As one can see from Fig. 6 predictions of the model agree very well with the data, only slight overestimation of protons and antiprotons can be observed but for the very low p_T region results agree within

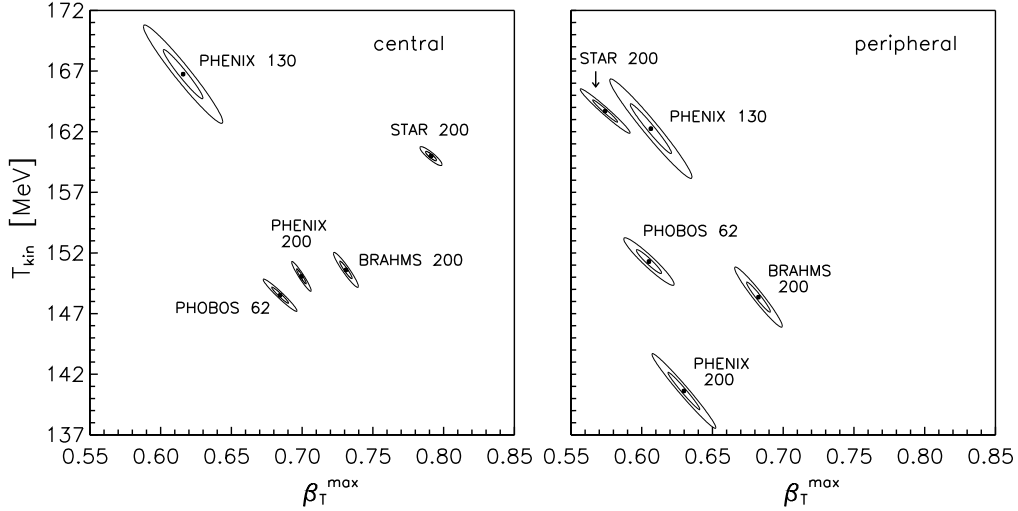


FIG. 2: The χ^2 contours (1σ and 2σ) in the parameter plain T_{kin} and β_{\perp}^{max} fixed by taking μ_B and τ at their optimum values. In the right panel the PHENIX case at $\sqrt{s_{NN}} = 130$ GeV is represented by the second from the most peripheral bin, see text for explanations. Dots denotes the optimum values of T_{kin} and β_{\perp}^{max} .

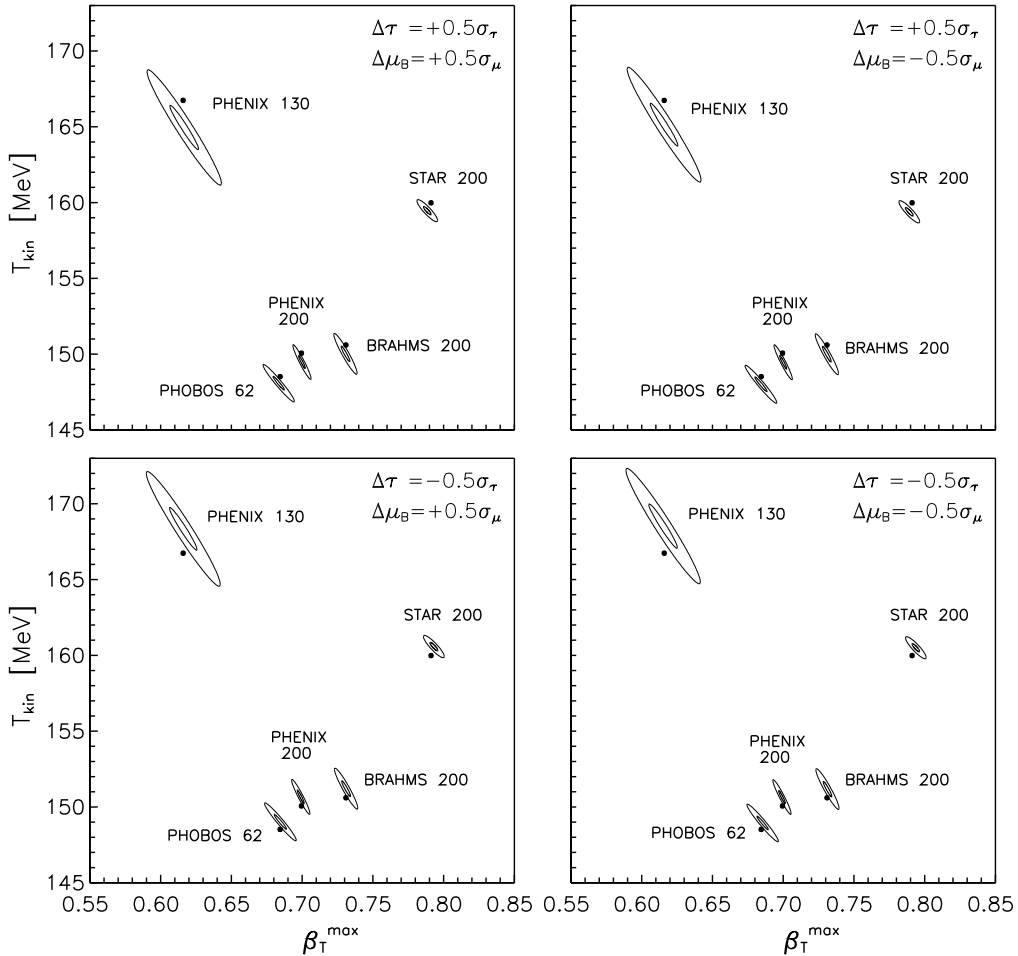


FIG. 3: The χ^2 contours (1σ and 2σ) in the parameter plains T_{kin} and β_{\perp}^{max} fixed by taking μ_B and τ at $\pm 0.5\sigma$ from their optimum values, $\Delta\tau = \tau - \tau_{opt}$, $\Delta\mu_B = \mu_B - \mu_{B,opt}$. All cases represent the most central classes. Dots denotes the optimum values of T_{kin} and β_{\perp}^{max} .

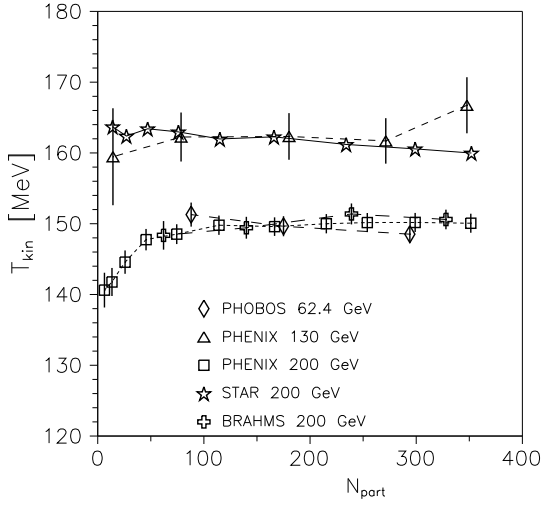


FIG. 4: Centrality dependence of the kinetic freeze-out temperature for the RHIC measurements at $\sqrt{s_{NN}} = 62.4, 130$ and 200 GeV. The lines connect the results and are a guide.

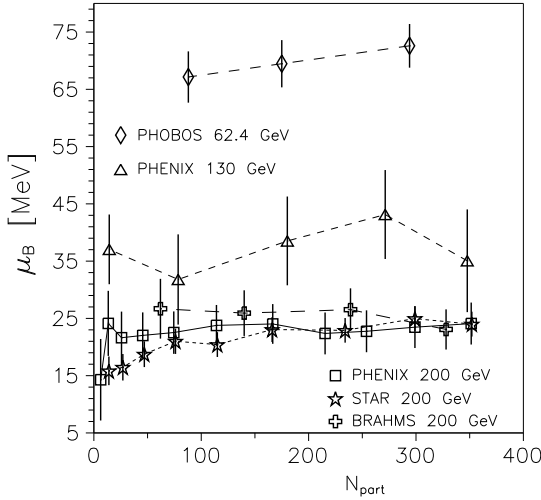


FIG. 5: Centrality dependence of the baryon number chemical potential for the RHIC measurements at $\sqrt{s_{NN}} = 62.4, 130$ and 200 GeV. The lines connect the results and are a guide.

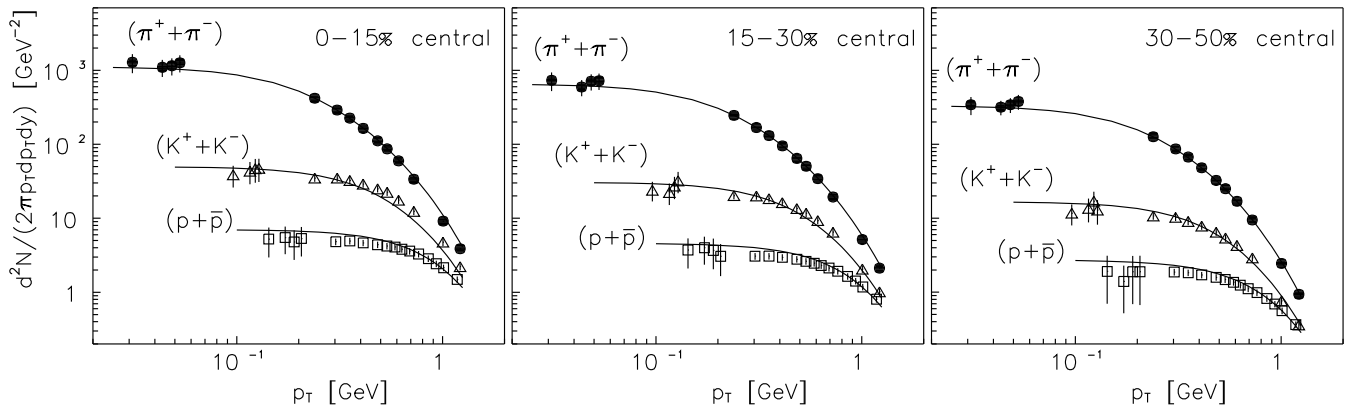


FIG. 6: Invariant yields as a function of p_T in Au+Au collisions at $\sqrt{s_{NN}} = 62.4$ GeV. Lines are predictions of the present model and symbols are PHOBOS data [17].

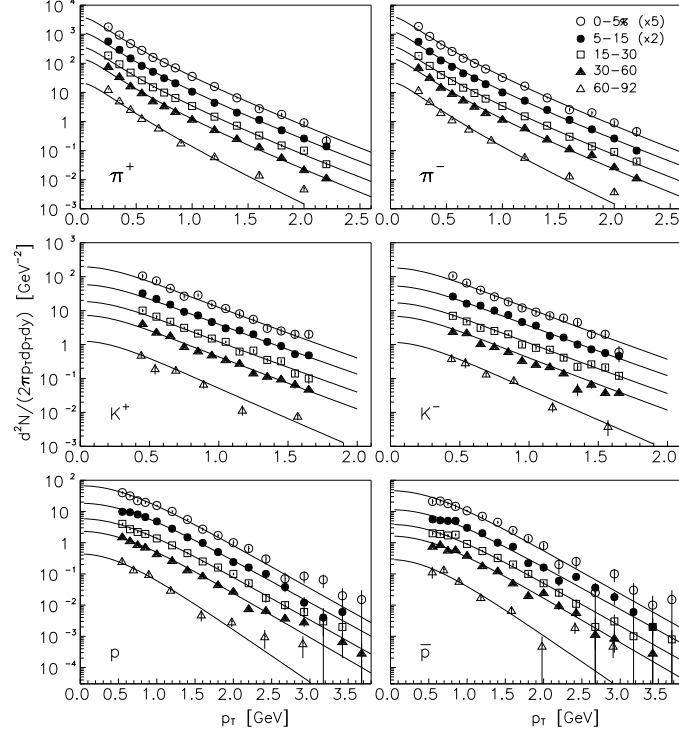


FIG. 7: Invariant yields as a function of p_T in Au+Au collisions at $\sqrt{s_{NN}} = 130$ GeV. Lines are predictions of the present model and symbols are PHENIX data [14]. For clarity, the data points are scaled vertically for two bins as quoted in the figure.

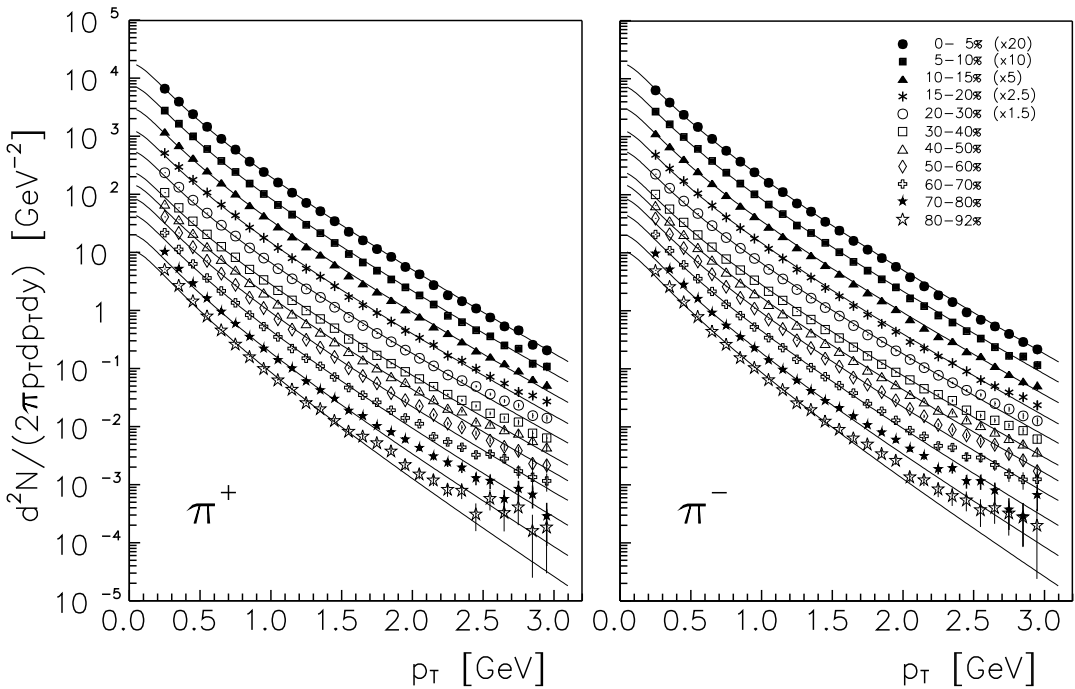


FIG. 8: Invariant yields of π^+ (left) and π^- (right) as a function of p_T in Au+Au collisions at $\sqrt{s_{NN}} = 200$ GeV. Lines are predictions of the present model and symbols are PHENIX data [24]. For clarity, the data points are scaled vertically for five bins as quoted in the figure.

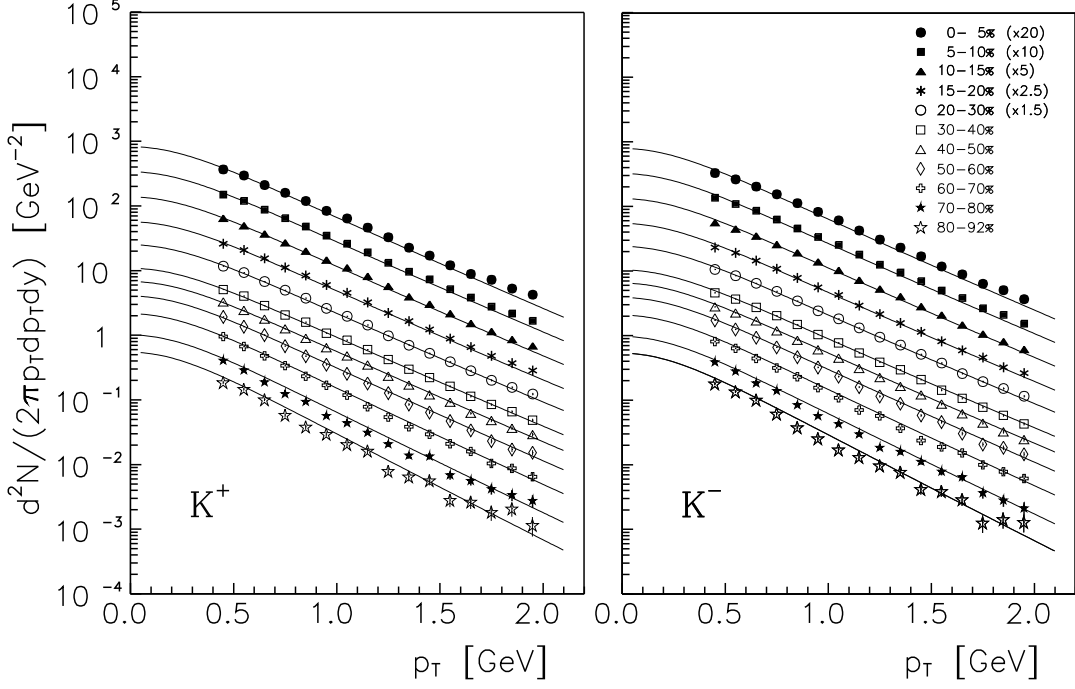


FIG. 9: Invariant yields of K^+ (left) and K^- (right) as a function of p_T in Au+Au collisions at $\sqrt{s_{NN}} = 200$ GeV. Lines are predictions of the present model and symbols are PHENIX data [24]. For clarity, the data points are scaled vertically for five bins as quoted in the figure.

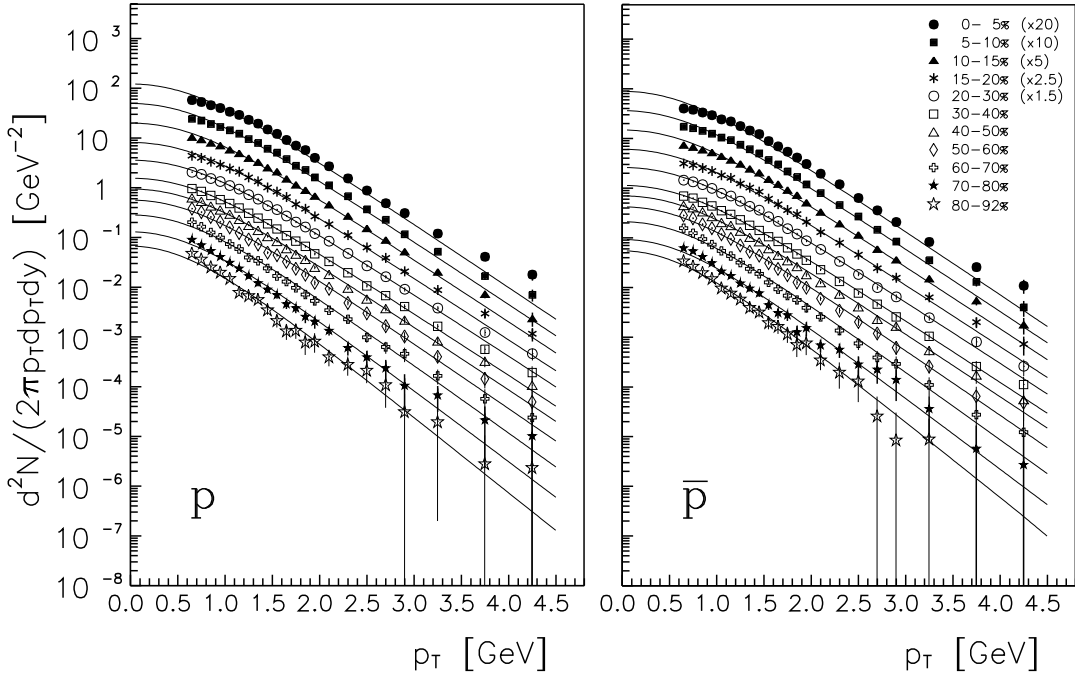


FIG. 10: Invariant yields of protons (left) and anti-protons (right) as a function of p_T in Au+Au collisions at $\sqrt{s_{NN}} = 200$ GeV. Lines are predictions of the present model and symbols are PHENIX data [24]. For clarity, the data points are scaled vertically for five bins as quoted in the figure.

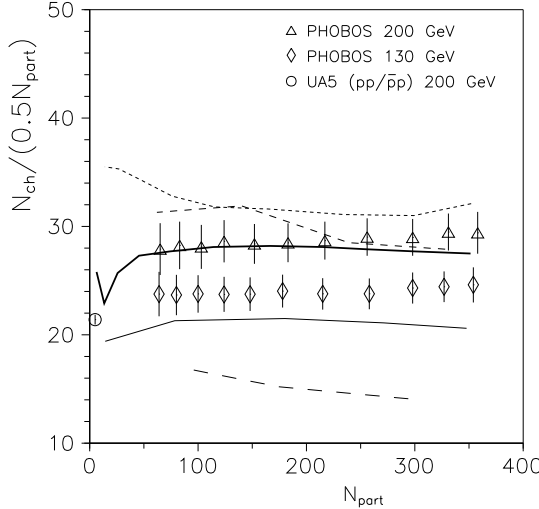


FIG. 11: N_{ch} per pair of participants versus N_{part} for RHIC at $\sqrt{s_{NN}} = 62.4, 130$ and 200 GeV. Lines are predictions of the model for the following experiments: STAR at $\sqrt{s_{NN}} = 200$ GeV (short-dashed), BRAHMS at $\sqrt{s_{NN}} = 200$ GeV (dashed), PHENIX at $\sqrt{s_{NN}} = 200$ GeV (thick solid), PHENIX at $\sqrt{s_{NN}} = 130$ GeV (thin solid) and PHOBOS at $\sqrt{s_{NN}} = 62.4$ GeV (long-dashed) . The PHOBOS data are from [26] and the $pp/\bar{p}p$ data point of the UA5 measurement is from Fig.39.5 in [21].

errors. Predictions of the blast-wave model also agree with the data (cf. Fig. 7 in [17]), but opposite to the present analysis, they underestimate pion yields and correctly estimate proton and antiproton yields at very low p_T . For the collisions at $\sqrt{s_{NN}} = 130$ GeV, Fig. 7, predictions for pion and kaon spectra agree very well with the PHENIX data, whereas for protons and antiprotons the agreement holds up to $p_T \approx 2.5$ GeV. Similar results were obtained within the blast-wave model (cf. Fig. 19 in [14]). In Figs. 8-10 results and data are presented for the PHENIX measurements at $\sqrt{s_{NN}} = 200$ GeV. Predictions for pions, Fig. 8, agree very well with the data practically in the whole p_T range for the first five bins from the top, for the next bins the predictions start to miss the data at $p_T \approx 2.5$ GeV and this value is decreasing with the centrality to $p_T \approx 2$ GeV for the most peripheral bin. Kaons are reproduced very well in the whole range of p_T and for all centralities, as one can see in Fig. 9. Protons and antiprotons agree very well up to $p_T \approx 3.3$ GeV for first nine bins from the top, for the two last peripheral bins the agreement is lost at $p_T \approx 2.5$ GeV, as it is seen in Fig. 10.

As a simple test of the self-consistency of the model the total charged-particle multiplicity, N_{ch} , has been estimated. The reasons for choosing N_{ch} are as follows: it is measured independently of hadron spectroscopy and in the whole rapidity range [26] and is given by a simple formula in the model. Namely, the total multiplicity of particle species i can be derived in the form

$$\begin{aligned} N_i &= \int d^2 p_T dy \frac{dN_i}{d^2 p_T dy} = \int d^2 p_T dy \int p^\mu d\sigma_\mu f_i(p \cdot u) = \int d\sigma \int d^2 p_T dy (p \cdot u) f_i(p \cdot u) \\ &= \int d\sigma \int \frac{d^3 \vec{p}}{E} (p \cdot u) f_i(p \cdot u) = \int d\sigma n_i(T, \mu_B) = n_i(T, \mu_B) \int d\sigma , \end{aligned} \quad (10)$$

if $d\sigma_\mu \sim u_\mu$ and the local thermal parameters are constant on the freeze-out hypersurface as it is here. Note that $n_i(T, \mu_B)$ is not the primordial thermal density of particle species i but it collects also contributions from decays of resonances and for estimations of measured N_{ch} one takes $i = \pi^+, \pi^-, K^+, K^-, p, \bar{p}$. Formally Eq. (10) means the integration of the invariant distribution given by Eq. (7) over the whole momentum space. So the dependence of the first integral on the statistical parameters is hidden in the appropriate dependence of the invariant distribution. But this invariant distribution has been used to fit parameters of the model and its best shape which matches the data is for optimum values of the parameters as tabulated in Table I. Of course, T and μ_B , now written explicitly as arguments of $n_i(T, \mu_B)$ in the last expression of Eq. (10) are exactly the same as those hidden in the first integral. Calculating the volume of the hypersurface [the last integral in Eq. (10)] and summing over all finally measured charged hadrons, one arrives at $N_{ch} = 2\pi \alpha_{||}^{max} \tau \rho_{max}^2 n_{ch}(T, \mu_B)$, where $n_{ch}(T, \mu_B)$ is the final charged particle density for a static gas and $\alpha_{||}^{max}(c) = y_p - \frac{\langle \delta y \rangle}{0.975} \cdot (1 - c)$ is the maximal value of the rapidity of the fluid element, y_p is the projectile rapidity, $\langle \delta y \rangle$ the average rapidity loss and c is a fractional number representing the middle of a given centrality bin, i.e. $c = 0.025$ for the $0 - 5\%$ centrality bin, etc. (for details see Ref. [25]). The BRAHMS Collaboration reports

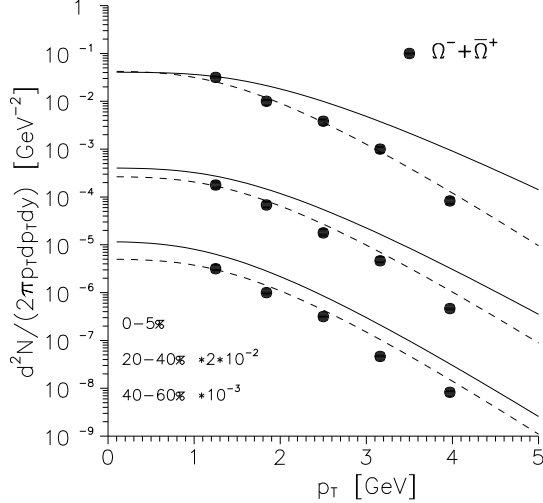


FIG. 12: Transverse momentum distributions of $\Omega^- + \bar{\Omega}^+$ for $|y| < 0.75$ in Au-Au collisions at $\sqrt{s_{NN}} = 200$ GeV. Data are from [28] (STAR) scaled for clarity, (statistical) errors are of the size of symbols. Lines denote model predictions: solid based on fits to the STAR spectra, dashed based on fits to the PHENIX spectra.

$\langle\delta y\rangle = 2.05$ for the 5% most central collisions at $\sqrt{s_{NN}} = 200$ GeV ($y_p = 5.36$) [27]. The results presented as the total charged-particle multiplicity per participating pair versus N_{part} are gathered in Fig. 11. The predictions for PHENIX and STAR exhibit almost ideal centrality independence within the range of the PHOBOS measurement [26], i.e. $N_{part} \approx 60 - 360$. For BRAHMS and PHOBOS predictions some dependence can be observed but changes are within 10% over all the range. Also predicted values agree well with the data for both PHENIX cases, whereas for others agree within $\approx 10\%$.

Another simple test of the model can be performed with the use of the spectra of Ω hyperon. This is because Ω has only the thermal contribution to the invariant distribution, Eq. (7). Such a test has been done for the blast-wave model [10] and for the single-freeze-out model [12], but in both cases the comparison was done with preliminary data. Present results together with the STAR data for $\Omega^- + \bar{\Omega}^+$ production at $\sqrt{s_{NN}} = 200$ GeV are shown in Fig. 12. Values of parameters for 20 – 40% and 40 – 60% centrality bins explored by STAR in Ω measurements are the averages of the values from Table I for bins which added percent coverage equals 20 – 40% and 40 – 60%, respectively. One can see that predictions based on fits to PHENIX spectra agree well with the data. Predictions based on fits to STAR spectra agree only qualitatively, they have higher normalization. Also for the 0 – 5% bin the slope differs. Blast-wave model predictions for $\Omega^- + \bar{\Omega}^+$ spectrum for the 0 – 5% bin of the preliminary STAR data were done in Ref. [10], but they do not agree with the data neither in normalization nor in a slope. The probable reason for the worse agreement of the STAR data based predictions in the present model, Fig. 12, is that STAR spectra of identified stable hadrons are measured in narrower ranges of p_T than PHENIX ones, i.e. $p_T \in [0.2, 1.2]$ GeV/c approximately for STAR [9] whereas for PHENIX $p_T \in [0.25, 2.95]$ GeV/c (pions), $p_T \in [0.55, 1.95]$ GeV/c (kaons) and $p_T \in [0.65, 4.25]$ GeV/c [(anti)protons] [24]. And the STAR measurement of $\Omega^- + \bar{\Omega}^+$ is done within the range $p_T \in [1.25, 4]$ GeV/c, practically outside the STAR range of p_T of identified stable hadrons but covering in great part PHENIX p_T ranges. Also they differ in common ranges of p_T , namely STAR spectra are placed slightly above the corresponding PHENIX spectra and in the case of pions have different slopes (it has been checked carefully for the common 0 – 5% bin after conversion of STAR spectra from $m_T - m_i$ to p_T , see Fig. 13). Actually, the difference in pion spectra is even greater than what is seen in Fig. 13, because the STAR pion spectra are corrected for weak decays [9]. Proton and antiproton spectra are not compared, since the PHENIX subtracted protons (antiprotons) from Λ ($\bar{\Lambda}$) decays, so by definition the STAR proton (antiproton) spectra are above the PHENIX ones. Also that the STAR minimizations have lower χ^2/NDF than PHENIX ones is probably because it is much easier to fit over a narrower range of p_T . Discrepancies between STAR and PHENIX spectra explain why the optimum values of parameters are different for these collaborations. These discrepancies could be caused by the different detectors used by the aforementioned Collaborations. The PHENIX uses a spectrometer, which consists of drift chamber (DC), pad chamber (PC) and time-of-flight (TOF) [24], whereas the STAR uses time projection chamber (TPC) [9]. The TPC is better in measurements of resonances but the PHENIX spectrometer measures spectra of identified particles more precisely [8, 33]. This might also help to understand why $\Omega^- + \bar{\Omega}^+$ measured spectra (an example of the STAR data on resonance production) are well reproduced in the model with the use of the parameters fitted to the PHENIX data on identified stable hadrons (in addition to the earlier argument based on the compatibility of p_T ranges).

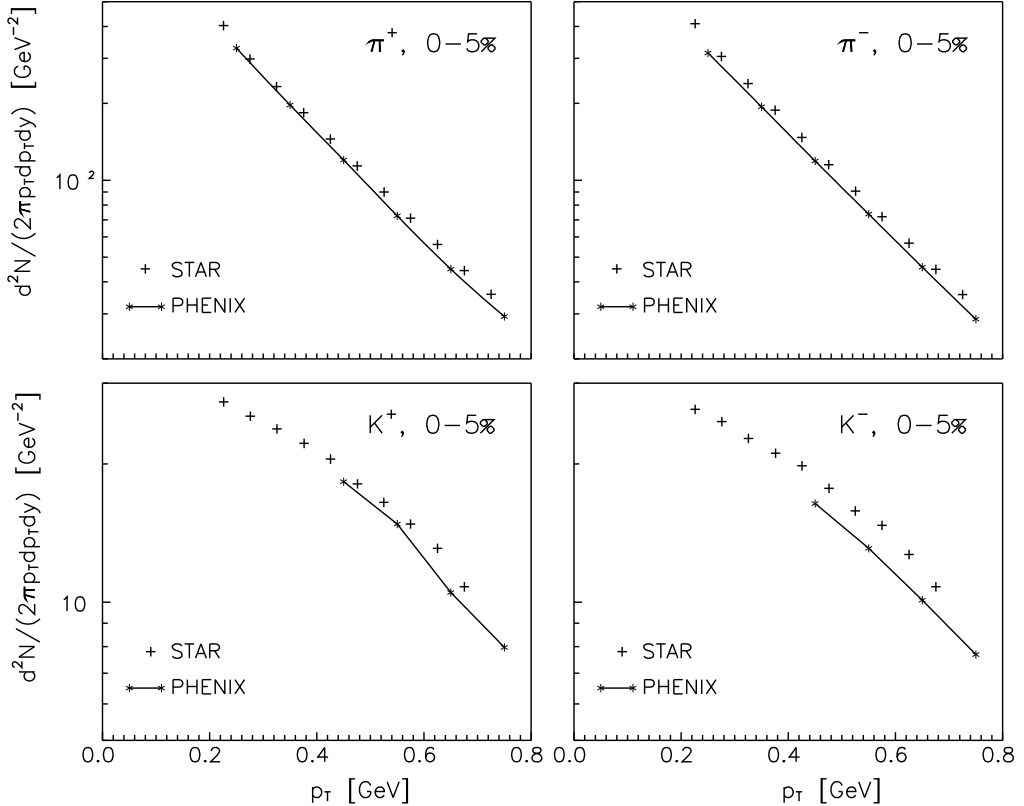


FIG. 13: Comparison of π^+ , π^- , K^+ and K^- spectra measured by STAR and PHENIX for the $0 - 5\%$ centrality bin at $\sqrt{s_{NN}} = 200$ GeV. All STAR data points are depicted, whereas PHENIX data ranges are cut from the right side (in fact they extend to $p_T = 2.95$ GeV for pions and $p_T = 1.95$ GeV for kaons).

IV. DISCUSSION AND CONCLUSIONS

Before the final conclusion one result of Ref. [2] should be commented. In [2] a hydrodynamical model supplemented with the dynamical freeze-out criterium [29, 30, 31]

$$\frac{1}{\tau_{scatt}} = \xi \frac{1}{\tau_{exp}} = \xi \partial_\mu u^\mu, \quad (11)$$

where $1/\tau_{scatt}$ is the local scattering rate and $1/\tau_{exp}$ is the local expansion rate and $\xi \sim 1$, was successfully used to explain the centrality dependence and the temperature range of T_{kin} determined from the blast-wave fits to the STAR data at $\sqrt{s_{NN}} = 200$ GeV [9]. To obtain the T_{kin} range comparable with the STAR results, $T_{kin} \simeq 90 - 130$ MeV, the appropriate adjustment of the parameter ξ was done, $\xi = 0.295$. Then, the range $T_{kin} \simeq 105 - 135$ MeV was obtained in [2]. Generally, hydrodynamics can be applied for $\tau_{scatt}^{-1} \gg \tau_{exp}^{-1}$ but when $\tau_{scatt}^{-1} \ll \tau_{exp}^{-1}$ certainly a system is no longer statistical [31]. However the determination of the strict border between a flow and a free stream of particles is somehow arbitrary, it is commonly accepted that on this border $\tau_{scatt}^{-1} \sim \tau_{exp}^{-1}$. Both rates decrease when the system cools down, but τ_{scatt}^{-1} is falling steeper, so it cuts τ_{exp}^{-1} at some temperature (it would represent the case $\xi = 1$; for some examples of simulations of τ_{scatt} and τ_{exp} see e.g. Ref. [32]). For the expansion rate multiplied by ξ , if $\xi < 1$ then $\xi \tau_{exp}^{-1}$ cuts τ_{scatt}^{-1} at some lower temperature, if $\xi > 1$ it happens at some higher temperature. Therefore, the choice $\xi = 0.295$ as in [2] means decreasing the freeze-out temperature so as it falls into the blast-wave range. Thus it is very likely that increasing ξ but still keeping $\xi \sim 1$ one could obtain the freeze-out temperature in the range $T_{kin} \simeq 140 - 165$ MeV as in the present model. Another point is the centrality dependence of T_{kin} . The change of T_{kin} with the centrality, of the order of 25% between the most central and the most peripheral bins, was obtained from Eq. (11) in [2], with the same expression for τ_{scatt}^{-1} taken for all centrality classes. Such assumption might not be reasonable, since e.g. in Ref. [30] variation of the temperature dependence of τ_{scatt} with specific entropy $S/A = s/n_B$ (entropy density per baryon number density) was shown, see Fig. 7 there. The specific entropy, as an

initial condition, could be different for each centrality class, so the different expression for τ_{scatt}^{-1} should be put into Eq. (11) in each case. Moreover, the scattering rate was calculated for pions only in a pion-kaon mixture [31]. The full scattering rate should include interactions between all constituents of the gas. Of course, this is an open question how such realistic scattering rate could influence the centrality dependence of T_{kin} determined from Eq. (11), but that this might flatten the dependence can not be excluded. And the last remark, T_{kin} points described as the STAR data [9] in Fig. 3 of Ref. [2] are not the measured quantities! They are blast-wave-fit results. Thus Fig. 3 in [2] demonstrates that T_{kin} obtained within the model where the freeze-out takes place on a hypersurface of constant temperature is consistent with the average T_{kin} for the hypersurface on where the temperature is not constant. Isn't that a bit of a contradiction?

In summary, the competitive hydrodynamical model has been proposed to describe hadronic p_T spectra measured at relativistic heavy-ion collisions. So far, conclusions about chemical and thermal (kinetic) freeze-outs have been drawn from the blast-wave parametrization of the final stage of the collision [18]. It has turned out that those conclusions are not definite and depend strongly on the applied model. In the present model the temperature and the baryon number chemical potential at the kinetic freeze-out are almost independent of the centrality of the collision and their values are very close to the values at the chemical freeze-out, what is opposite to the conclusions drawn from the blast-wave model analysis [2]. Such behavior justifies the *ad hoc* assumption about one freeze-out postulated in Refs. [19, 20].

Acknowledgments

This work was supported in part by the Polish Ministry of Science and Higher Education under contract No. N N202 0953 33.

[1] U. Heinz, Nucl. Phys. A **661**, 140 (1999).
 [2] U. Heinz and G. Kestin, arXiv:nucl-th/0612105.
 [3] G. Torrieri and J. Rafelski, J. Phys. Conf. Ser. **5**, 246 (2005) [arXiv:hep-ph/0409160].
 [4] M. Kaneta and N. Xu, presented at QM2004 (Oakland) (only at arXiv:nucl-th/0405068).
 [5] W. Florkowski, W. Broniowski and M. Michalec, Acta Phys. Polon. B **33**, 761 (2002).
 [6] J. Cleymans, B. Kampfer, M. Kaneta, S. Wheaton and N. Xu, Phys. Rev. C **71**, 054901 (2005).
 [7] P. Braun-Munzinger, D. Magestro, K. Redlich and J. Stachel, Phys. Lett. B **518**, 41 (2001).
 [8] J. Rafelski, J. Letessier and G. Torrieri, Phys. Rev. C **72**, 024905 (2005).
 [9] J. Adams *et al.* [STAR Collaboration], Phys. Rev. Lett. **92**, 112301 (2004).
 [10] O. Y. Barannikova [STAR Collaboration], presented at QM2004 (Oakland) (only at arXiv:nucl-ex/0403014).
 [11] O. Barannikova [STAR Collaboration], J. Phys. G **31**, S93 (2005).
 [12] A. Baran, W. Broniowski and W. Florkowski, Acta Phys. Polon. B **35**, 779 (2004).
 [13] P. Braun-Munzinger, K. Redlich and J. Stachel, in *Quark-Gluon Plasma 3*, eds R. C. Hwa and Xin-Nian Wang (World Scientific Publishing, Singapore, 2004), p. 491.
 [14] K. Adcox *et al.* [PHENIX Collaboration], Phys. Rev. C **69**, 024904 (2004).
 [15] J. M. Burward-Hoy [PHENIX Collaboration], Nucl. Phys. A **715**, 498 (2003).
 [16] I. Arsene *et al.* [BRAHMS Collaboration], Phys. Rev. C **72**, 014908 (2005).
 [17] B. B. Back *et al.* [PHOBOS Collaboration], Phys. Rev. C **75**, 024910 (2007).
 [18] E. Schnedermann, J. Sollfrank and U. Heinz, Phys. Rev. C **48**, 2462 (1993).
 [19] W. Broniowski and W. Florkowski, Phys. Rev. Lett. **87**, 272302 (2001).
 [20] W. Broniowski and W. Florkowski, Phys. Rev. C **65**, 064905 (2002).
 [21] K. Hagiwara *et al.* [Particle Data Group Collaboration], Phys. Rev. D **66**, 010001 (2002).
 [22] W. Broniowski, A. Baran and W. Florkowski, Acta Phys. Polon. B **33**, 4235 (2002).
 [23] D. Prorok, Eur. Phys. J. A **24**, 93 (2005).
 [24] S. S. Adler *et al.* [PHENIX Collaboration], Phys. Rev. C **69**, 034909 (2004).
 [25] D. Prorok, Phys. Rev. C **73**, 064901 (2006).
 [26] B. B. Back *et al.* [PHOBOS Collaboration], Phys. Rev. C **74**, 021902(R) (2006).
 [27] I. G. Bearden *et al.* [BRAHMS Collaboration], Phys. Rev. Lett. **93**, 102301 (2004).
 [28] J. Adams *et al.* [STAR Collaboration], Phys. Rev. Lett. **98**, 062301 (2007).
 [29] J. P. Bondorf, S. I. A. Garpman and J. Zimanyi, Nucl. Phys. A **296**, 320 (1978).
 [30] E. Schnedermann and U. W. Heinz, Phys. Rev. C **50**, 1675 (1994).
 [31] C. M. Hung and E. V. Shuryak, Phys. Rev. C **57**, 1891 (1998).
 [32] G. Bertsch, M. Gong, L. D. McLerran, P. V. Ruuskanen and E. Sarkkinen, Phys. Rev. D **37**, 1202 (1988).
 [33] J. Rafelski (private communication).